Receiver Function Investigation of Crustal Structure in the Malawi and Luangwa Rift Zones and Adjacent Areas

Muchen Sun[1,2], Stephen S. Gao[2], Kelly H. Liu[2], Kevin Mickus[3], & Xiaofei Fu[1]

[1]College of Earth Science and Research Institute of Unconventional Oil and Gas, Northeast Petroleum University, Daqing, Heilongjiang, China.

[2]Geology and Geophysics Program, Missouri University of Science and Technology, Rolla, Missouri, USA.

[3]Department of Geography, Geology, and Planning, Missouri State University, Springfield, Missouri, USA.

Key Points:

- Crustal thickness and V_p/V_s in the vicinity of the Malawi and Luangwa rift zones are measured using receiver functions
- Low V_p/V_s measurements along the western edge of the northern Malawi rift are attributable to infiltration of magma-derived CO_2
- Elevated V_p/V_s in southern Malawi rift suggests partial melting, and normal crustal thickness and V_p/V_s for Luangwa are observed

Corresponding author: Stephen S. Gao, sgao@mst.edu

Abstract

Stacking over 2500 P-to-S receiver functions recorded by 34 broadband seismic stations installed in the vicinity of the Malawi and Luangwa rift zones (MRZ and LRZ, respectively) reveals significant variations of crustal thickness (33.4-46.1 km) and V_p/V_s (1.69-1.84). The resulting crustal stretching factor is about 1.1 for the MRZ, which is approximately 10 - 40% lower than that observed in the mature segments of the East African rift system (EARS). The V_p/V_s ratio is high (≥ 1.81) beneath the southern MRZ, indicating the possible existence of partial melting. Low V_p/V_s values of 1.69-1.71 are observed along the western boundary of the northern MRZ and are attributable to infiltration of magma-derived CO_2 in the crust. The LRZ shows negligible crustal thinning and a V_p/V_s that is comparable to the globally averaged value for continental crust, suggesting a complete recovery of crustal properties in terms of crustal thickness and V_p/V_s.

1 Introduction

A typical continental rift is a fault-bounded narrow valley where the entire lithosphere has been pulled apart under extension (Gregory, 1894; Sengor & Burke, 1978). One of the most common features in continental rifts is basaltic volcanism, which originates from either partial melting in the lithosphere or plume upwelling from the sub-lithospheric mantle (Sengor & Burke, 1978). A recent ambient noise tomographic (ANT) study (Wang et al., 2019) suggests that, in continental rifts, the magnitude of crustal thinning has a close relationship with the development of rift-related volcanisms. Different from most of the mature segments of the East Africa Rift System (EARS) which have been studied extensively using various techniques, the non-volcanic Cenozoic Malawi rift and the Paleozoic-Mesozoic Luangwa rift (Ebinger et al., 2017) have been inadequately investigated. Consequently, the magnitude and extent of crustal deformation, the existence of partial melting or mafic intrusion in the crust, and important characteristics such as the depth penetration and possible CO_2 infiltration of the seismically active boundary faults, remain enigmatic.

Laboratory investigations of crustal rock samples (Holbrook et al., 1992) suggest that under average crustal temperature and pressure conditions, felsic, intermediate, and mafic rocks have V_p/V_s values of smaller than 1.76, between 1.76 and 1.81, and greater than 1.81, respectively. The existence of crustal partial melting can lead to a higher V_p/V_s

due to a greater reduction of V_s than V_p (Greenfield et al., 2016). Similarly, the intensive intrusion of mantle materials into the crust can also increase the bulk crust V_p/V_s (Christensen, 1996). Moreover, an increasing number of mineral physical and observational studies have suggested that CO_2 released from the mantle through deep and steep lithospheric faults (Lee et al., 2016) can significantly reduce crustal V_p/V_s (Julian et al., 1998; Parmigiani et al., 2016; Roecker et al., 2017). CO_2 can decrease V_p through its strong effect on the pore-fluid compressibility of the crustal porous rock, and consequently, reduce the crustal V_p/V_s (Ito et al., 1979; Mavko & Mukerji, 1995). Therefore, observations of V_p/V_s values that are below the normal felsic rock value of 1.76 may suggest the presence of magma-derived CO_2, and that of lithospheric faults acting as conduits for the CO_2 (Lee et al., 2016) .

In this study, we present measurements from a receiver function study using recently recorded broadband seismic data that we collected as part of an interdisciplinary investigation (Gao et al., 2013) to unveil the crustal characteristics and impact of CO_2 and partial melting on V_p/V_s beneath the Malawi and Luangwa rift zones (MRZ and LRZ, respectively) and adjacent areas.

2 Tectonic Setting

The Cenozoic MRZ is the southernmost segment of the magma-poor western branch of the EARS. It separates the Nubian plate and the Rovuma microplate (Figure 1) and originated approximately 25 Ma (Roberts et al., 2012). The Rungwe Volcanic Province located at the northern tip of the rift zone is the only volcanic province within the MRZ (Ebinger et al., 1993). Kinematic GPS studies (Saria et al., 2014; Stamps et al., 2018) indicated that the spreading rate between the Nubian plate and the Rovuma microplate decreases gradually from the northern tip (2.2 mm/yr) to the southern tip (1.5 mm/yr) of the MRZ. One of the most controversial issues beneath the MRZ is the existence of thermal upwelling from lower mantle. Broadband seismic studies using the same data set used by this study have shown that there is a normal mantle transition zone thickness (Reed et al., 2016) and a NE-SW oriented seismic azimuthal anisotropy (Reed et al., 2017) under the rift, suggesting that there is no significant rift-related mantle flow and detectable influence of an active plume in the vicinity of the mantle transition zone. Some geodynamic modeling studies also inferred a lack of observable thermal upwelling from the lower mantle beneath the MRZ, and favor an upper mantle origin of rifting (Stamps et al., 2014; 2015). In contrary, a recent seismic anisotropy study (Tepp et al., 2018) attributed the NE oriented azimuthal anisotropy observed in the MRZ to horizontal mantle flow that is enhanced by weak thermal upwelling from the lower mantle beneath southern Africa. Similarly, the existence of an active mantle plume from the lower mantle beneath southern Africa was suggested by seismic tomography (Mulibo & Nyblade, 2013; Ritsema et al., 1999) and geodynamic modeling studies (Gurnis et al., 2000; Lithgow-Bertelloni & Silver, 1998). Relative to the mantle, the crust beneath most part of the MRZ has been inadequately studied. A recent receiver function study for the northern MRZ and the Rungwe Volcanic Province (Borrego et al., 2018) suggests a bulk felsic to intermediate crustal composition and small variation of crustal thickness, and concludes that crustal thinning in the northern MRZ is highly focused beneath the center of the rifted basin.

Another major tectonic feature in East Africa is the Permo-Triassic LRZ, which has been reactivated probably by the same stress field responsible for the formation of the Cenozoic EARS (Banks et al., 1995; Fritz et al., 2013). The Luangwa rifting started in earliest Permian times and ended in the Triassic (Banks et al., 1995; Daly et al., 1989; Fritz et al., 2013). The southwestern segment of the LRZ follows the ENE-trending Mwembeshi Shear Zone, which separates the Proterozoic Irumide Belt and the South Irumide Belts (SIB), while its northeastern portion is situated in the Irumide Belt (Figure 1). Geochronological studies by Johnson et al. (2005; 2006) indicate that different magmatic events resulted in a significant distinction of the crustal characteristics between these two neighboring orogenic belts. The Mwembeshi Shear Zone separates the lithosphere between the Irumide Belt and SIB, which is evidenced by the observation of an electrically conductive discontinuity in the mantle (Sarafian et al., 2018). This conductive discontinuity might represent a suture zone which is a result of collision between two lithospheric fragments after subduction of an oceanic slab beneath the Irumide Belt (Johnson et al., 2007; Sarafian et al., 2018). Previous integrated studies consider that the left lateral movement on the Mwembeshi Shear Zone dominated the development of the LRZ, while subsequent right lateral movement resulted in rifting inversions (Banks et al., 1995; Daly et al., 1989; Orpen et al., 1989).

3 Data and Methods

The teleseismic (epicentral distance ranging from 30° to 180°) data used in the study were recorded by 34 stations (Figure 1) that we installed in Malawi, Mozambique, and Zambia over a 2 year period (2012 - 2014) as a component of the SAFARI (Seismic Arrays for African Rift Initiation; Gao et al., 2013) project. To balance the quality and quantity of the selected data, a variable cut-off magnitude (M_c) was set by $M_c = 5.2 + (\Delta - 30.0)/(180.0 - 30.0) - D/700.0$ where Δ and D are the epicentral distance in degree and focal depth in kilometer, respectively (Liu & Gao, 2010). A band-pass filter with a frequency range between 0.04 - 0.8 Hz was applied to the seismograms, which were windowed 20 s before and 260 s after the theoretical first P-wave arrival based on the IASP91 Earth model (Kennett & Engdahl, 1991). If the signal to noise ratio (S/N) of the first arrival on the vertical component was greater than 4.0, the filtered seismograms were selected to generate P-to-S receiver functions (RFs) following the procedure of Ammon (1991) with a water level value of 0.03. The resulting P-to-S RFs for each of the stations were inspected visually to reject the ones without a clear first P-arrival in the first 2 second window. A total of 2504 high-quality radial RFs from 311 events were selected for determining crustal thickness (H) and V_p/V_s (κ).

3.1 H-κ Stacking

Following the H-κ stacking procedure of Zhu & Kanamori (2000), the selected RFs were moveout corrected and stacked to grid-search for the optimal pair of the crustal thickness and V_p/V_s, which corresponds to the maximum stacking amplitude. We search for the maximum amplitude in the depth range of 25-50 km with an interval of 0.1 km, and in the V_p/V_s range of 1.60-1.95 with an interval of 0.01. For two (W07CR and Z06GL) of the 34 stations, the search ranges are adjusted to select the peak corresponding to an H-κ pair that is comparable to the neighboring stations. H-κ plots for all the 34 stations can be found in Figures S1-S34. In this study, a crustal mean P-wave velocity of 6.1 km/s was chosen for the H-κ stacking, which is consistent with the IASP91 Earth model. It is worth noting that the mean crustal velocity assumed has a positive correlation with the resulting crustal thickness, and a negative correlation with the resulting V_p/V_s ratio. Specifically, a 1% increase of mean crustal velocity assumed can lead to an $\sim$0.46 km increase in the resulting crustal thickness and an $\sim$0.0024 reduction in the resulting V_p/V_s ratio, respectively (Nair et al., 2006). Subsequently, following a bootstrap resampling procedure (Efron & Tibshirani, 1986), the mean and standard deviation of the measurements for each station were calculated.

A delay time of approximately 0.4 s of the first arrivals and strong multiple reflections in the RFs are observed at one of the stations (Z06GL) located in the LRZ, which is caused by the presence of a low-velocity (relative to that of the bedrock) sedimentary layer (Yu et al., 2015). Such strong reverberations can mask the P-to-S converted phases from the Moho. For this station, we determined the two-way travel time of the reverberations and designed a resonance-removal filter in the frequency domain to remove the reverberations and to isolate the P-to-S converted phases from the Moho (Yu et al., 2015).

3.2 RF Migration

To produce a spatially continuous image of the Moho, we migrated the RFs and projected them into a rift orthogonal (W-E) and a rift parallel (S-N) profile, respectively. To produce the cross-sections, the RF raypaths were computed using an assumed mean crustal V_p of 6.1 km/s and the optimal mean crustal V_p/V_s value for each station obtained from H-κ stacking. We then divided the 25-55 km depth range of the Earth along the profile into rectangular blocks of 1° (longitude for the W-E profile, and latitude for the S-N profile) by 1 km (vertical) with a horizontal and vertical moving step of 0.1° and 0.1 km, respectively. The mean amplitude of the RFs with raypaths in each of the rectangular blocks was calculated and the stacked RFs were normalized by the maximum amplitude in the 25-55 km depth range.

4 Results

Robust P-to-S arrivals are obtained from the migrated RFs (Figure 2), enabling reliable determinations of crustal thickness and V_p/V_s beneath the vast majority of the stations.

4.1 Crustal Thickness and V_p/V_s From H-κ Stacking

The resulting crustal thicknesses vary from 33.4 km beneath the northern part of the MRZ to 46.1 km beneath the Mozambique belt with an average of 41.5 ± 2.7 km (Figure 3a), and the V_p/V_s values range from 1.69 to 1.84 with a mean value of 1.75 ± 0.04 (Figure 3b). Along the rift-orthogonal profile, the crustal thickness in the MRZ is

2 - 3 km thinner than the surrounding orogenic belts (Figure 2a and 3a). The Mozambique Belt has an average thickness of 42.3 ± 2.7 km and V_p/V_s of 1.78 ± 0.04. The mean crustal thickness of the SIB is 43.6 ± 0.6 km, while the V_p/V_s measurements have a mean value of 1.75 ± 0.01. H-κ stacking from 6 stations in the Irumide Belt leads to a mean crustal thickness of 41.1 ± 1.9 km and V_p/V_s of 1.73 ± 0.03. For the two stations situated in the LRZ, the crustal thickness is 43.3 km at Z06GL and 44.6 km at Z08MF, and the V_p/V_s is 1.75 at both stations.

Along the rift-parallel profile, the averaged crustal thickness is 39.6 ± 2.6 km (Figure 3a). The thinnest crust (33.4 km) was found beneath Station W07CR at the northern end of the profile, while the thickest crust (43.2 km) was observed at Station Z03 in the central part of the MRZ (Figure 3a). The resulting V_p/V_s values observed beneath MRZ fall within the range of 1.69 - 1.84 with an average of 1.74 ± 0.05 (Figure 3b). Small V_p/V_s values were revealed at 6 stations (W07CR, W08KB, W09TK, W05SL, W11KP, and W10LW) in the northern half of the S-N profile, ranging from 1.69 to 1.71, with a mean of 1.70 ± 0.01.

The measurements of crustal thickness along two profiles in this study are consistent with that from several neighboring stations in previous RF studies (Borrego et al., 2018; Kachingwe et al., 2015). Using data from 39 broadband seismic stations, the crustal structure beneath southern Africa was investigated using receiver functions (Kachingwe et al., 2015). Three of their stations were approximately along our profiles. A crustal thickness of 34.7 km was reported at Station MZM, which was located between our stations W07CR and W08KB at which crustal thicknesses of 33.4 ± 0.25 km and 39.9 ± 0.49 km were obtained, respectively. However, the V_p/V_s (1.81) reported at Station MZM (Kachingwe et al., 2015) is larger than those from W07CR (1.69 ± 0.01) and W08KB (1.70 ± 0.01). The crustal thickness and V_p/V_s determined at Station ZOMB are 38.3 km and 1.78 (Kachingwe et al., 2015), respectively, while our results are 37.8 ± 0.30 km and 1.83 at Station W14MC which was co-sited with ZOMB. Similarly, the crustal thickness and V_p/V_s reported by Kachingwe et al. (2015) beneath Station SERJ are 45.2 km and 1.71, which are similar to the 43.2 ± 0.72 km and 1.73 ± 0.01 values reported at a nearby station (Station Z03CK) in this study.

Another receiver function study (Borrego et al., 2018), which focused on the northern MRZ and the Rungwe Volcanic Province, had two stations near our stations. The crustal thickness at LIVA is 36.0 km, which is about 2 km larger than the crustal thickness of 33.4 ± 0.25 km observed by our adjacent station W07CR, and the V_p/V_s at Station LIVA (1.72) is comparable with that obtained by Station W07CR (1.69). Similarly, for station THAN, the reported crustal thickness is 42.5 km, which is slightly larger than the crustal thickness of 39.9 km that we observed at neighboring station W08KB. The V_p/V_s values between the two stations are comparable (1.67 at THAN and 1.70 at W08KB). Note that Borrego et al. (2018) used a mean crustal V_p of 6.3 km/s which is greater than the 6.1 km/s that we used which may have led to a crustal thickness that is about 2 km greater for the former (Nair et al., 2006).

4.2 Moho Depth Variation From Migrated RFs

The spatial variation of crustal thickness and its correspondence with surface elevation is visible on the migrated and laterally smoothed RF profiles (Figure 2). Along the rift-orthogonal profile (Figures 2a and 2c), the western boundary of the LRZ separates the LRZ with a thick crust and the Irumide Belt with relatively thin crust. Contrasting to the commonly observed correspondence between thicker crust and higher elevations, the Irumide Belt, which has a thinner crust, is characterized by an elevation that is more than 1 km higher than the LRZ. Additionally, although the Irumide Belt and the SIB have similar elevations, the crust beneath the latter is a few km thicker.

A different relationship between crustal thickness and surface elevation is revealed in the eastern half of the rift-orthogonal profile, where a thicker crust corresponds to a higher elevation. For instance, the MRZ, which has the lowest elevation in the study area, corresponds to a crustal thinning of a few kilometers relative to the adjacent SIB, and the high elevation area on the Mozambique Belt adjacent to the MRZ is characterized by a thick crust. A sudden thinning of the crust further east corresponds to a significant elevation reduction.

The along-rift variation of crustal thickness is delineated by the migrated RFs (Figure 2d). The major features include a crustal thickening at the high-elevation southern terminus of the MRZ, as well as a sudden crustal thinning beneath the northern end of the profile. Caution must be taken that for stations northern of 14°S, the stations were located on the western edge of the MRZ, while the rest of the stations along the NS profile were approximately in the axial area (Figure 1). Therefore, if the area with the maximum crustal thinning is limited underneath the surface expression of the rift, the observed crustal thickness beneath the northern stations might be larger than the axial area. However, it is worth to realize that the difference in the resulting crustal thickness between Station W05SL, which, similar to the rest of the northern stations, was on the rift shoulder, and Station W06SB, which was approximately in the axial area, is less than 3 km.

5 Discussion

5.1 Constraints on Crustal Magmatic Intrusion and Partial Melting Beneath the MRZ

Borrego et al. (2018) observed negligible crustal thinning beneath the shoulder of the northern MRZ, suggesting that crustal thinning in the northern MRZ must be highly focused beneath the centers of rift basin segments. In this study, a relatively flat Moho (39.6 ± 2.6 km) was found under most stations in the MRZ including the central and southern parts of the MRZ. The average crustal thickness observed beneath the Mozambique Belt and SIB are 42.3 ± 2.7 km and 43.6 ± 0.6 km, respectively, which are consistent with the ≥ 40 km results from a recent ANT study (Wang et al., 2019). Therefore, along the rift-orthogonal profile, the crustal thickness in the MRZ is 2 - 3 km thinner than the surrounding orogenic belts (Figure 2a and 3a), leading to a stretching factor (β) factor of about 1.1, which is about 10 - 40% lower than that observed in the mature segments of the EARS (Plasman et al., 2017; Reed et al., 2014; Stuart et al., 2006). Here, the stretching factor is defined as the ratio between the initial crustal thickness and the final crustal thickness (Park, 1997). This stretching factor seems to indicate that, relative to other parts of the EARS, crustal thinning within the MRZ is relatively minor even within the central portion of the MRZ. This relatively low magnitude crustal thinning beneath the MRZ is consistent with the absence of volcanism on the surface except for the Rungwe Volcanic Province.

In contrast to the small variations of crustal thickness along the axis of the MRZ, the resulting V_p/V_s values observed within the MTZ varies greatly from 1.69 at the northernmost part to 1.84 in the central part of the MRZ (Figure 3b), implying significant along-rift variations of crustal composition, degree of partial melting, or temperature. The high V_p/V_s (≥ 1.81) determined at stations Q01MP, W06SB, and W14MC (Figure 3b), which are situated in the central and southern parts of the MRZ, implies the possible existence of magmatic intrusion in the lower crust or partial melting in the crust beneath some areas of the MRZ. Higher-than-normal V_s in the crust is expected, if the high V_p/V_s is caused by magmatic intrusion in the crust from mantle. However, the recent ANT study (Wang et al., 2019) revealed lower-than-normal V_s beneath these areas. All these observations, when combined with the evidence of the absence of crustal thickening from magmatic addition observed in this study (Figure 2b), are inconsistent with the possibility of the presence of magmatic intrusion of high-density mantle material into the crust beneath the central and southern parts of the MRZ.

Broadband seismic studies have observed a normal mantle transition zone thickness (Reed et al., 2016) and NE-SW oriented seismic azimuthal anisotropy which is similar to that observed across the rest of southern Africa (Reed et al., 2017; Silver et al., 2001), suggesting that absence of rifting-related mantle flow beneath the MRZ. These observations suggest that the high V_p/V_s values could be related to partial melting and elevated temperatures induced by lithospheric stretching decompression rather than ascending magma from an active mantle plume.

5.2 Infiltration of Magma-Derived CO_2 in the Crust beneath the Northern MRZ

Anomalously low V_p/V_s values ranging from 1.69 to 1.71 with a mean value of 1.70 $\pm$ 0.01 were determined at six stations (W05, W07, W08, W09, W10, and W11) along the western boundary of the MRZ. The most commonly cited cause for such low V_p/V_s values is the presence of rocks with a high silicon content (Christensen, 1996), which, to our knowledge, is not found by previous studies in the study area. A recently proposed alternate mechanism for low V_p/V_s is magma-derived CO_2 in the crustal porous rock. CO_2 can decrease V_p through its strong effect on the pore-fluid compressibility of the crustal porous rock, and consequently, reduce the crustal V_p/V_s, an observation that is supported by both elasticity theory (Mavko & Mukerji, 1995) and experiments (Ito et al., 1979). Based on the observation that the V_p/V_s in the area with massive CO_2 outgassing beneath Mammoth Mountain (California) is about 9% lower than surrounding rocks, Julian et al. (1998) also suggested that the anomaly low V_p/V_s could be a diagnostic feature of magma-derived CO_2 degassing.

Magma-derived CO_2 can be released from the sub-continental lithosphere through deeply penetrating extensional fault systems (e.g., Foly & Fischer, 2017; Julian et al., 1998; Parmigiani et al., 2016; Roecker et al., 2017), which potentially makes the EARS an important source area in the Earth deep carbon cycle (Burton et al., 2013). Parmigiani et al. (2016) suggest that a magmatic volatile phase is prone to migrate from the crystal-rich regions to the crystal-poor parts, and accumulate large volumes of low density bubbles at the roof of the crystal-poor magma reservoir. Therefore, the deep boarder and intra-rift faults beneath the the rift zones, if they connect to the magma reservoir in the sub-continental lithosphere, could be infiltrated by the magma-derived volatiles (Foly & Fischer, 2017; Roecker et al., 2017). The high CO_2 flux data in the fault zones reveals that the deep lithospheric fault system in the EARS does act as permeable conduits for transporting magma-derived CO_2 (Lee et al., 2016).

Considering the enormous quantity of recently recognized CO_2 outgassing along the faults in the EARS (Lee et al., 2016) and similar observations of low V_p/V_s values along the edges of the EARS in northern Tanzania and southern Kenya (Roecker et al., 2017), we speculate that a viable explanation for the anomalously low V_p/V_s observed in the northern part of the MRZ is caused by the infiltration of magma-derived CO_2 in the crust.

5.3 Post-Rifting Recovery of Crustal Thickness and V_p/V_s of the LRZ

Unlike the tectonically active MRZ, the resulting crustal thickness beneath the Paleozoic-Mesozoic LRZ, the southern part of which was developed in the Mwembeshi Shear Zone, is not significantly thinner than that beneath the adjacent orogenic belts. It has been widely recognized that regional compression can lead to cessation of rifting and if the compressional stress persists for a longer time, to recovery of the original crustal thickness (Stein et al., 2018), leading to rift inversion. Additionally, reduction in rifting-related high temperature anomalies and disappearance of crustal partial melting may cause the reduction of the V_p/V_s anomaly associated with rifting.

The formation of the LRZ and its subsequent inversion can be related to strike slip movements along the Mwembeshi Shear Zone. Left lateral movement associated with continental collision along the Mwembeshi Shear Zone formed the LRZ in earliest Permian times, while later right lateral movements, which changed regional stress pattern from extension to compression in the vicinity of the LRZ, led to post-rifting inversion (Banks et al., 1995). In spite of the currently higher level of tectonic activity relative to the surrounding areas and the speculation that the LRZ has been reactivated (Banks et al., 1995; Daly et al., 1989; Orpen et al., 1989), the observed negligible crustal thinning and insignificant variation of V_p/V_s beneath the LRZ relative to the surrounding area suggest that post-rifting inversion of the LRZ has possibly completed since the cessation of the rifting event.

6 Conclusions

Crustal thickness and V_p/V_s beneath 34 SAFARI stations located along two profiles in the vicinity of the MRZ and LRZ were imaged by stacking 2504 high-quality RFs. The crustal thickness measurements are generally consistent with sparsely spaced previous measurements. The new observations show that relative to the adjacent orogenic belts, the crust beneath the MRZ is thinned by about 3 km. This low magnitude crustal stretching is consistent with the absence of volcanisms in the main portions of the MRZ. Some areas in the MRZ show a high crustal V_p/V_s of 1.81 or greater, which, when combined with the observations from other broadband seismic studies may indicate the existence of partial melting probably associated with lithospheric stretching decompression. One of the most significant observations from this study is the spatially consistent low V_p/V_s measurements in the range of 1.69 - 1.71 along the western edge of the northern MRZ, which could be interpreted by the infiltration of magma-derived CO_2 into the crust. Based on the negligible crustal thinning and insignificant variation of V_p/V_s beneath the LRZ relative to the surrounding area, we propose that the post-rifting inversion of the LRZ has possibly completed, and the recent reactivation of tectonic activities in the failed rift represents localization of regional strain along preexisting zones of mechanical weakness in the rifted crust.

Acknowledgments

We thank the IRIS DMC for archiving the data used in the study, and the Portable Array Seismic Studies of the Continental Lithosphere Instrument Center for providing equipment and logistical support. All the data used in the study were obtained from the IRIS DMC (last accessed: August 2018). Field assistance provided by Cory Reed, Shane Ingate, Patrick R. N. Chindandali, Belarmino Massingue, Hassan Mdala, and Daniel Mutamina, as well as by various government agencies and universities in Malawi, Mozambique, and Zambia are greatly appreciated. This study was partially supported by the U.S. National Science Foundation under grants 1009946 and 1460516 to S.G. and K.L., and by the China Scholarship Council to M.S. under award 201508230075.

References

[52] Ammon, C. J. (1991). The isolation of receiver effects from teleseismic *P*-waveforms. *Bulletin of the Seismological Society of America, 81*(6), 2504-2510.

[52] Banks, N. L., Bardwell, K. A., & Musiwa, S. (1995). Karoo rift basins of the Luangwa Valley, Zambia. *Geological Society, London, Special Publications, 80*(1), 285-295. https://doi.org/10.1144/GSL.SP.1995.080.01.13

[52] Borrego, D., Nyblade, A. A., Accardo, N. J., Gaherty, J. B., Ebinger, C. J., Shillington, D. J., et al. (2018). Crustal structure surrounding the northern Malawi rift and beneath the Rungwe Volcanic Province, East Africa. *Geophysical Journal International, 215*(2), 1410-1426. https://doi.org/10.1093/gji/ggy331

[52] Burton, M. R., Sawyer, G. M., & Granieri, D. (2013). Deep carbon emissions from volcanoes. *Reviews in Mineralogy and Geochemistry, 75*(1), 323-354. https://doi.org/10.2138/rmg.2013.75.11

[52] Christensen, N. I. (1996). Poisson's ratio and crustal seismology. *Journal of Geophysical Research: Solid Earth, 101*(B2), 3139-3156. https://doi.org/10.1029/95JB03446

[52] Daly, M. C., Chorowicz, J., & Fairhead, J. D. (1989). Rift basin evolution in Africa: the influence of reactivated steep basement shear zones. *Geological Society, London, Special Publications, 44*(1), 309-334. https://doi.org/10.1144/GSL.SP.1989.044.01.17

[52] Ebinger, C. J., Deino, A. L., Tesha, A. L., Becker, T., & Ring, U. (1993). Tectonic controls on rift basin morphology: evolution of the Northern Malawi (Nyasa) Rift. *Journal of Geophysical Research: Solid Earth, 98*(B10), 17821-17836. https://doi.org/10.1029/93JB01392

[52] Ebinger, C. J., Keir, D., Bastow, I. D., Whaler, K., Hammond, J. O., Ayele, A., et al. (2017). Crustal structure of active deformation zones in Africa: Implications for global crustal processes. *Tectonics, 36*(12), 3298-3332. https://doi.org/10.1002/2017TC004526

[52] Efron, B., & Tibshirani, R. (1986). Bootstrap methods for standard errors, confidence intervals, and other measures of statistical accuracy. *Statistical science*, 54-75.

[52] Foley, S. F., & Fischer, T. P. (2017). An essential role for continental rifts and lithosphere in the deep carbon cycle. *Nature Geoscience, 10*(12), 897. https://doi.org/10.1038/s41561-017-0002-7

[52] Fritz, H., Abdelsalam, M., Ali, K. A., Bingen, B., Collins, A. S., Fowler, A. R., et al. (2013). Orogen styles in the East African Orogen: a review of the Neoproterozoic to Cambrian tectonic evolution. *Journal of African Earth Sciences, 86*, 65-106. https://doi.org/10.1016/j.jafrearsci.2013.06.004

[52] Gao, S. S., Liu, K. H., Reed, C. A., Yu, Y., Massinque, B., Mdala, H., et al. (2013). Seismic arrays to study African rift initiation. *Eos, Transactions American Geophysical Union, 94*(24), 213-214. https://doi.org/10.1002/2013EO240002

[52] Greenfield, T., White, R. S., & Roecker, S. (2016). The magmatic plumbing system of the Askja central volcano, Iceland, as imaged by seismic tomography. *Journal of Geophysical Research: Solid Earth, 121*(10), 7211-7229. https://doi.org/10.1002/2016JB013163

[52] Gregory, J. W. (1894). Contributions to the physical geography of British East Africa. *The Geographical Journal, 4*, 289-315.

[52] Gurnis, M., Mitrovica, J. X., Ritsema, J., & van Heijst, H. J. (2000). Constraining mantle density structure using geological evidence of surface uplift rates: The case of the African superplume. *Geochemistry, Geophysics, Geosystems, 1*(7). https://doi.org/10.1029/1999GC000035

[52] Holbrook, W. S., Mooney, W. D., & Christensen, N. I. (1992). The seismic velocity structure of the deep continental crust. *Continental lower crust, 23*, 1-43.

[52] Ito, H., DeVilbiss, J., & Nur, A. (1979). Compressional and shear waves in saturated rock during water-steam transition. *Journal of Geophysical Research: Solid Earth, 84*(B9), 4731-4735. https://doi.org/10.1029/JB084iB09p04731

[52] Johnson, S. P., De Waele, B., & Liyungu, K. A. (2006). U-P$_b$ sensitive high-resolution ion microprobe (SHRIMP) zircon geochronology of granitoid rocks in eastern Zambia: Terrane subdivision of the Mesoproterozoic Southern Irumide Belt. *Tectonics, 25*(6). https://doi.org/10.1029/2006TC001977

[52] Johnson, S. P., De Waele, B., Tembo, F., Katongo, C., Tani, K., Chang, et al., (2007). Geochemistry, geochronology and isotopic evolution of the Chewore-Rufunsa Terrane, Southern Irumide Belt: a Mesoproterozoic continental margin arc. *Journal of Petrology, 48*(7), 1411-1441. https://doi.org/10.1093/petrology/egm025

[52] Johnson, S. P., Rivers, T., & De Waele, B. (2005). A review of the Mesoproterozoic to early Palaeozoic magmatic and tectonothermal history of south-central Africa: implications for Rodinia and Gondwana. *Journal of the Geological Society, 162*(3), 433-450. https://doi.org/10.1144/0016-764904-028

[52] Julian, B. R., Pitt, A. M., & Foulger, G. R. (1998). Seismic image of a CO_2 reservoir beneath a seismically active volcano. *Geophysical Journal International, 133*(1), F7-F10. https://doi.org/10.1046/j.1365-246X.1998.1331540.x

[52] Kachingwe, M., Nyblade, A., & Julia, J. (2015). Crustal structure of Precambrian terranes in the southern African subcontinent with implications for secular variation in crustal genesis. *Geophysical Journal International, 202*(1), 533-547. https://doi.org/10.1093/gji/ggv136

[52] Kennett, B. L. N., & Engdahl, E. R. (1991). Traveltimes for global earthquake location and phase identification. *Geophysical Journal International, 105*(2), 429-465. https://doi.org/10.1111/j.1365-246X.1991.tb06724.x

[52] Lee, H., Muirhead, J. D., Fischer, T. P., Ebinger, C. J., Kattenhorn, S. A., Sharp, Z. D., & Kianji, G. (2016). Massive and prolonged deep carbon emissions associated with continental rifting. *Nature Geoscience, 9*(2), 145. https://doi.org/10.1038/ngeo2622

[52] Liu, K. H., & Gao, S. S. (2010). Spatial variations of crustal characteristics beneath the Hoggar swell, Algeria, revealed by systematic analyses of receiver functions from a single seismic station. *Geochemistry, Geophysics, Geosystems, 11*(8). https://doi.org/10.1029/2010GC003091

[52] Lithgow-Bertelloni, C., & Silver, P. G. (1998). Dynamic topography, plate driving forces and the African superswell. *Nature, 395*(6699), 269. https://doi.org/10.1038/26212

[52] Mavko, G., & Mukerji, T. (1995). Seismic pore space compressibility and Gassmann's relation. *Geophysics, 60*(6), 1743-1749. https://doi.org/10.1190/1.1443907

[52] Mulibo, G. D., & Nyblade, A. A. (2013). The P and S wave velocity structure of the mantle beneath eastern Africa and the African superplume anomaly. *Geochemistry, Geophysics, Geosystems, 14*(8), 2696-2715. https://doi.org/10.1002/ggge.20150

[52] Nair, S. K., Gao, S. S., Liu, K. H., & Silver, P. G. (2006). Southern African crustal evolution and composition: Constraints from receiver function studies. *Journal of Geophysical Research: Solid Earth, 111*(B2). https://doi.org/10.1029/2005JB003802

[52] Orpen, J. L., Swain, C. J., Nugent, C., & Zhou, P. P. (1989). Wrench-fault and half-graben tectonics in the development of the Palaeozoic Zambezi Karoo Basins in Zimbabwe - the "Lower Zambezi" and "Mid-Zambezi" basins respectively - and regional implications. *Journal of African Earth Sciences (and the Middle East), 8*(2-4), 215-229. https://doi.org/10.1016/S0899-5362(89)80026-0

[52] Park, R. G. (1997). Foundation of structural geology. (3rd ed.) Psychology Press. p. 64.

[52] Parmigiani, A., Faroughi, S., Huber, C., Bachmann, O., & Su, Y. (2016). Bubble accumulation and its role in the evolution of magma reservoirs in the upper crust. *Nature, 532*(7600), 492. https://doi.org/10.1038/nature17401

[52] Plasman, M., Tiberi, C., Ebinger, C., Gautier, S., Albaric, J., Peyrat, S., et al. (2017). Lithospheric low-velocity zones associated with a magmatic segment of the Tanzanian Rift, East Africa. *Geophysical Journal International, 210*(1), 465-481. https://doi.org/10.1093/gji/ggx177

[52] Ritsema, J., van Heijst, H. J., & Woodhouse, J. H. (1999). Complex shear wave velocity structure imaged beneath Africa and Iceland. *Science, 286*(5446), 1925-1928. https://doi.org/10.1126/science.286.5446.1925

[52] Roecker, S., Ebinger, C., Tiberi, C., Mulibo, G., Ferdinand-Wambura, R., Mtelela, K., et al (2017). Subsurface images of the Eastern Rift, Africa, from the joint inversion of body waves, surface waves and gravity: investigating the role of fluids in early-stage continental rifting. *Geophysical Journal International, 210*(2), 931-950. https://doi.org/10.1093/gji/ggx220

[52] Reed, C. A., Almadani, S., Gao, S. S., Elsheikh, A. A., Cherie, S., Abdelsalam, M. G., et al. (2014). Receiver function constraints on crustal seismic velocities and partial melting beneath the Red Sea rift and adjacent regions, Afar

Depression. *Journal of Geophysical Research: Solid Earth, 119*(3), 2138-2152. https://doi.org/10.1002/2013JB010719

[52] Reed, C. A., Liu, K. H., Chindandali, P., Massingue, B., Mdala, H., Mutamina, D., et al. (2016). Passive rifting of thick lithosphere in the southern East African Rift: Evidence from mantle transition zone discontinuity topography. *Journal of Geophysical Research: Solid Earth, 121*(11), 8068-8079. https://doi.org/10.1002/2016JB013131

[52] Reed, C. A., Liu, K. H., Yu, Y., & Gao, S. S. (2017). Seismic anisotropy and mantle dynamics beneath the Malawi Rift Zone, East Africa. *Tectonics, 36*(7), 1338-1351. https://doi.org/10.1002/2017TC004519

[52] Roberts, E. M., Stevens, N. J., O'Connor, P. M., Dirks, P. H. G. M., Gottfried, M. D., Clyde, W. C., et al. (2012). Initiation of the western branch of the East African Rift coeval with the eastern branch. *Nature Geoscience, 5*(4), 289. https://doi.org/10.1038/ngeo1432

[52] Sarafian, E., Evans, R. L., Abdelsalam, M. G., Atekwana, E., Elsenbeck, J., Jones, A. G., & Chikambwe, E. (2018). Imaging Precambrian lithospheric structure in Zambia using electromagnetic methods. *Gondwana Research, 54*, 38-49. https://doi.org/10.1016/j.gr.2017.09.007

[52] Saria, E., Calais, E., Stamps, D. S., Delvaux, D., & Hartnady, C. J. H. (2014). Present-day kinematics of the East African Rift. *Journal of Geophysical Research: Solid Earth, 119*(4), 3584-3600. https://doi.org/10.1002/2013JB010901

[52] Sengor, A. M & Burke, K. (1978). Relative timing of rifting and volcanism on Earth and its tectonic implications. *Geophysical Research Letters, 5*(6), 419-421. https://doi.org/10.1029/GL005i006p00419

[52] Silver, P. G., Gao, S. S., Liu, K. H., & Kaapvaal Seismic Group. (2001). Mantle deformation beneath southern Africa. *Geophysical Research Letters, 28*(13), 2493-2496. https://doi.org/10.1029/2000GL012696

[52] Stamps, D. S., Flesch, L. M., Calais, E., & Ghosh, A. (2014). Current kinematics and dynamics of Africa and the East African Rift System. *Journal of Geophysical Research: Solid Earth, 119*(6), 5161-5186. https://doi.org/10.1002/2013JB010717

[52] Stamps, D. S., Iaffaldano, G., & Calais, E. (2015). Role of mantle flow in Nubia-Somalia plate divergence. *Geophysical Research Letters, 42*(2), 290-296.

https://doi.org/10.1002/2014GL062515

[52] Stamps, D. S., Saria, E., & Kreemer, C. (2018). A geodetic strain rate model for the East African Rift system. *Scientific reports, 8*(1), 732. https://doi.org/10.1038/s41598-017-19097-w

[52] Stein, S., Stein, C. A., Elling, R., Kley, J., Keller, G. R., Wysession, M., et al. (2018). Insights from North America's failed Midcontinent Rift into the evolution of continental rifts and passive continental margins. *Tectonophysics, 744*, 403-421. https://doi.org/10.1016/j.tecto.2018.07.021

[52] Stuart, G. W., Bastow, I. D., & Ebinger, C. J. (2006). Crustal structure of the northern Main Ethiopian Rift from receiver function studies. *Geological Society, London, Special Publications, 259*(1), 253-267. https://doi.org/10.1144/GSL.SP.2006.259.01.20

[52] Tepp, G., Ebinger, C. J., Zal, H., Gallacher, R., Accardo, N., Shillington, D. J., et al. (2018). Seismic anisotropy of the upper mantle below the Western rift, East Africa. *Journal of Geophysical Research: Solid Earth, 123*, 5644-5660. https://doi.org/10.1029/2017JB015409

[52] Wang, T., Feng, J., Liu, K. H., & Gao, S. S. (2019). Crustal structure beneath the Malawi and Luangwa Rift Zones and adjacent areas from ambient noise tomography. *Gondwana Research, 67*, 187-198. https://doi.org/10.1016/j.gr.2018.10.018

[52] Yu, Y., Song, J., Liu, K. H., & Gao, S. S. (2015). Determining crustal structure beneath seismic stations overlying a low-velocity sedimentary layer using receiver functions. *Journal of Geophysical Research: Solid Earth, 120*(5), 3208-3218. https://doi.org/10.1002/2014JB011610

[52] Zhu, L., & Kanamori, H. (2000). Moho depth variation in southern California from teleseismic receiver functions. *Journal of Geophysical Research: Solid Earth, 105*(B2), 2969-2980. https://doi.org/10.1029/1999JB900322

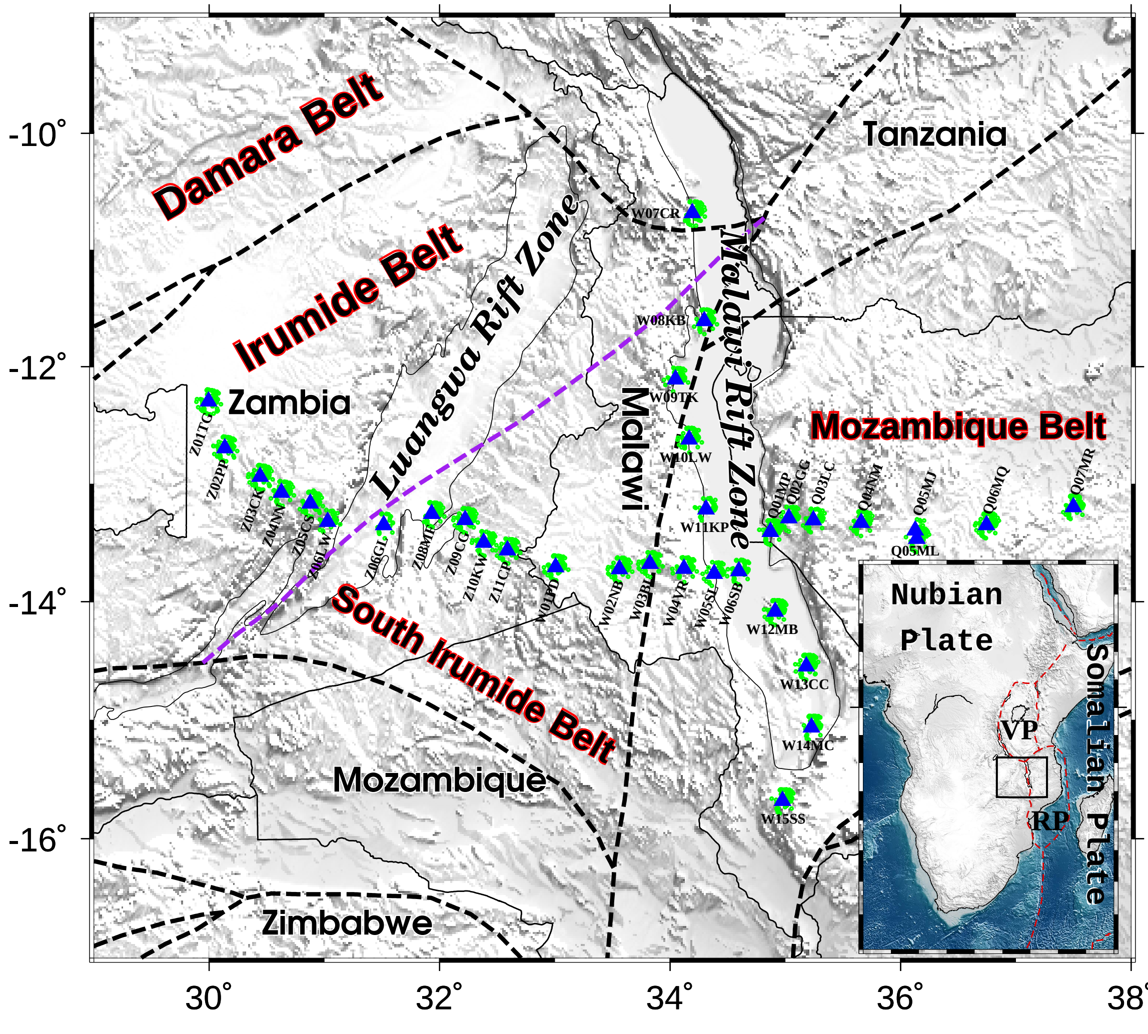

Figure 1. Topographic map of the study area showing the distribution of seismic stations (blue triangles) used in the study and major tectonic features. The green dots are ray-piercing points of P-to-S conversions at the depth of 41.5 km. The dashed lines show the tectonic boundaries, among which the purple dashed line is the Mwembeshi Shear Zone. The rectangle in the inset map indicates the study area.

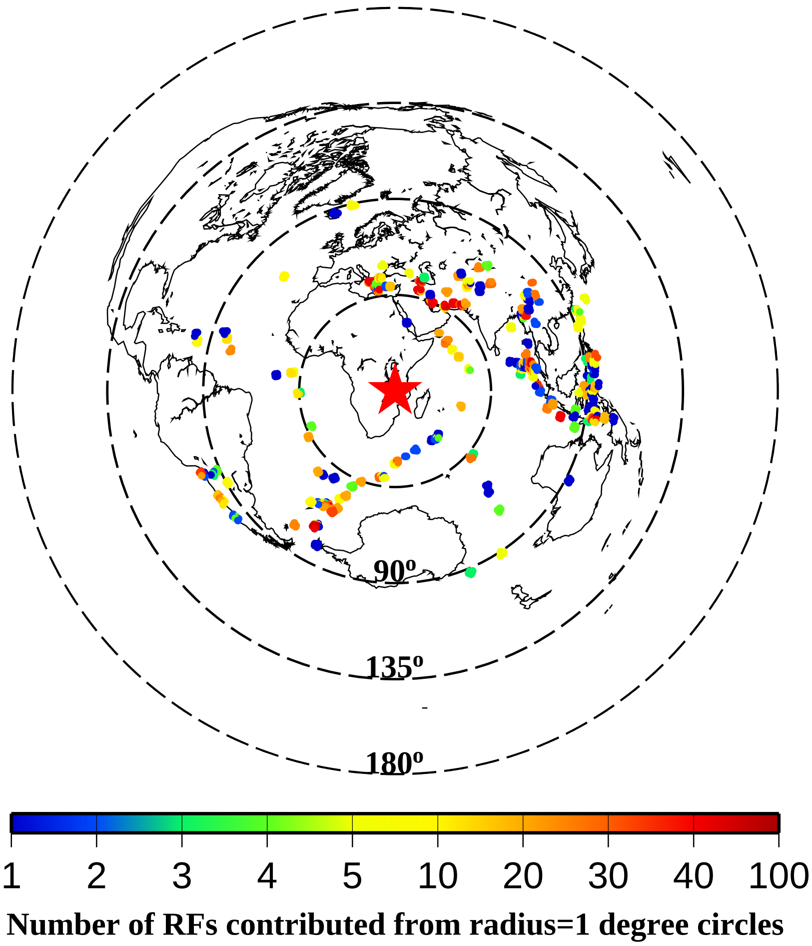

Figure 2. Spatial distribution of earthquake source areas. Each dot represents a radius = 1° circular area. The distance between neighboring circles is 1°. The color of the dot represents the number of used RFs originated from earthquakes in the circle. The radius of the concentric dashed circles centered at the central part of the study area (star) indicates the epicentral distance.

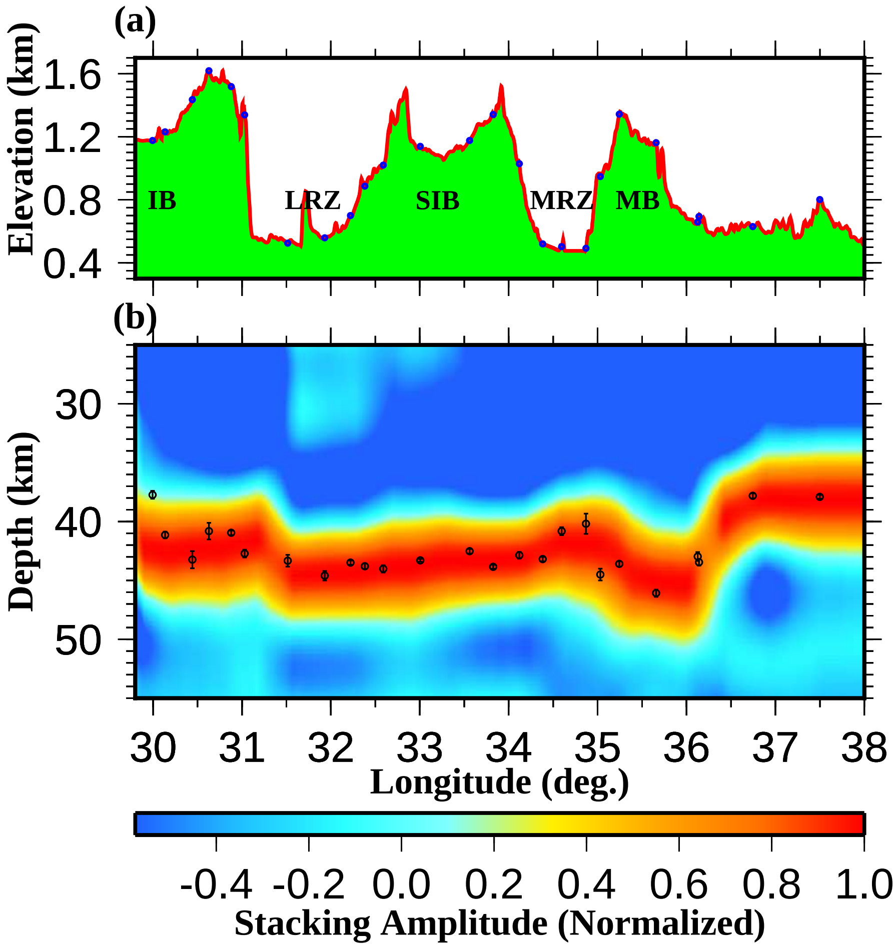

557 **Figure 3.** Surface elevation (top panel) and migrated receiver function profile (bottom panel)
558 along rift-orthogonal profile. The black dots indicate results from H-κ stacking.

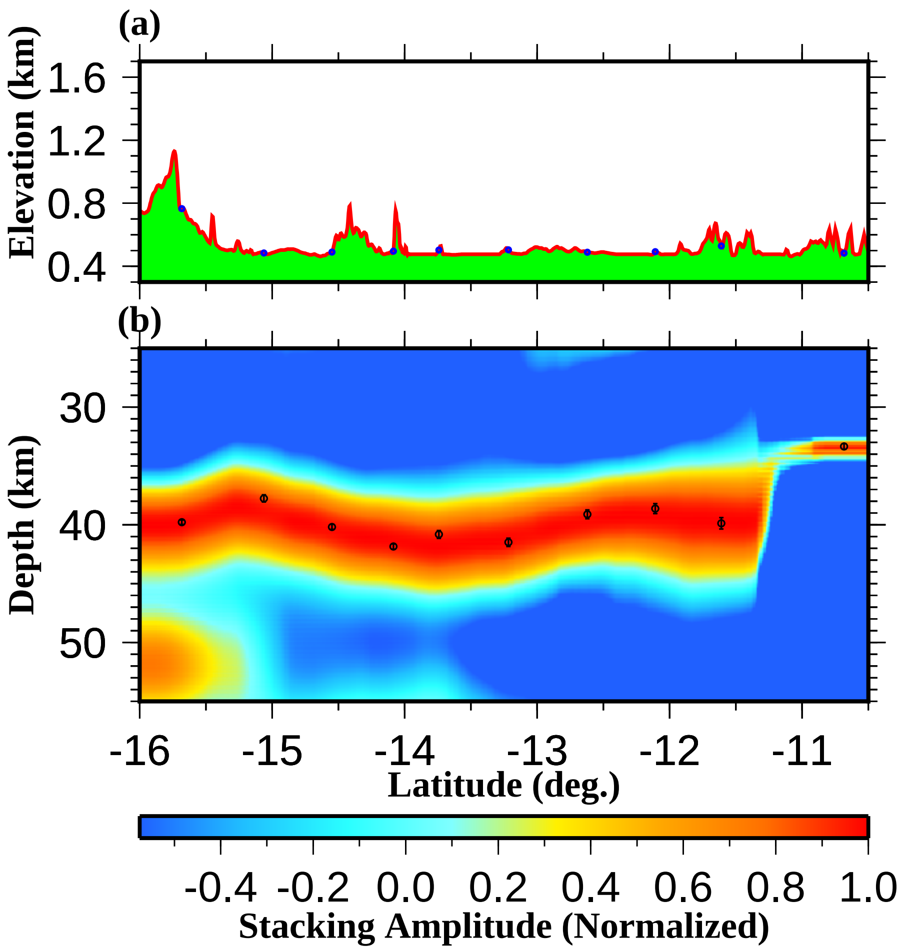

559 **Figure 4.** Same as Figure 3 but for the rift-parallel profile.

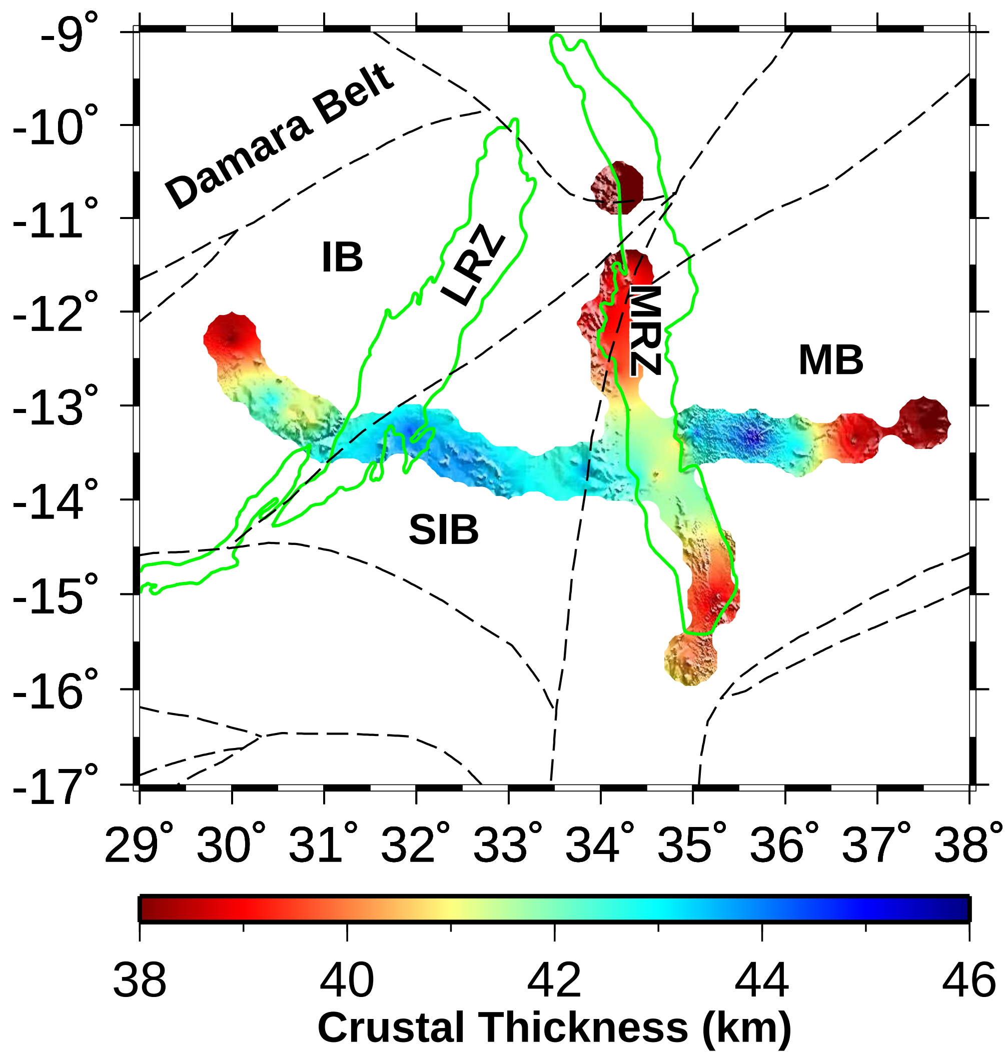

560 **Figure 5.** Distribution of resulting crustal thickness.

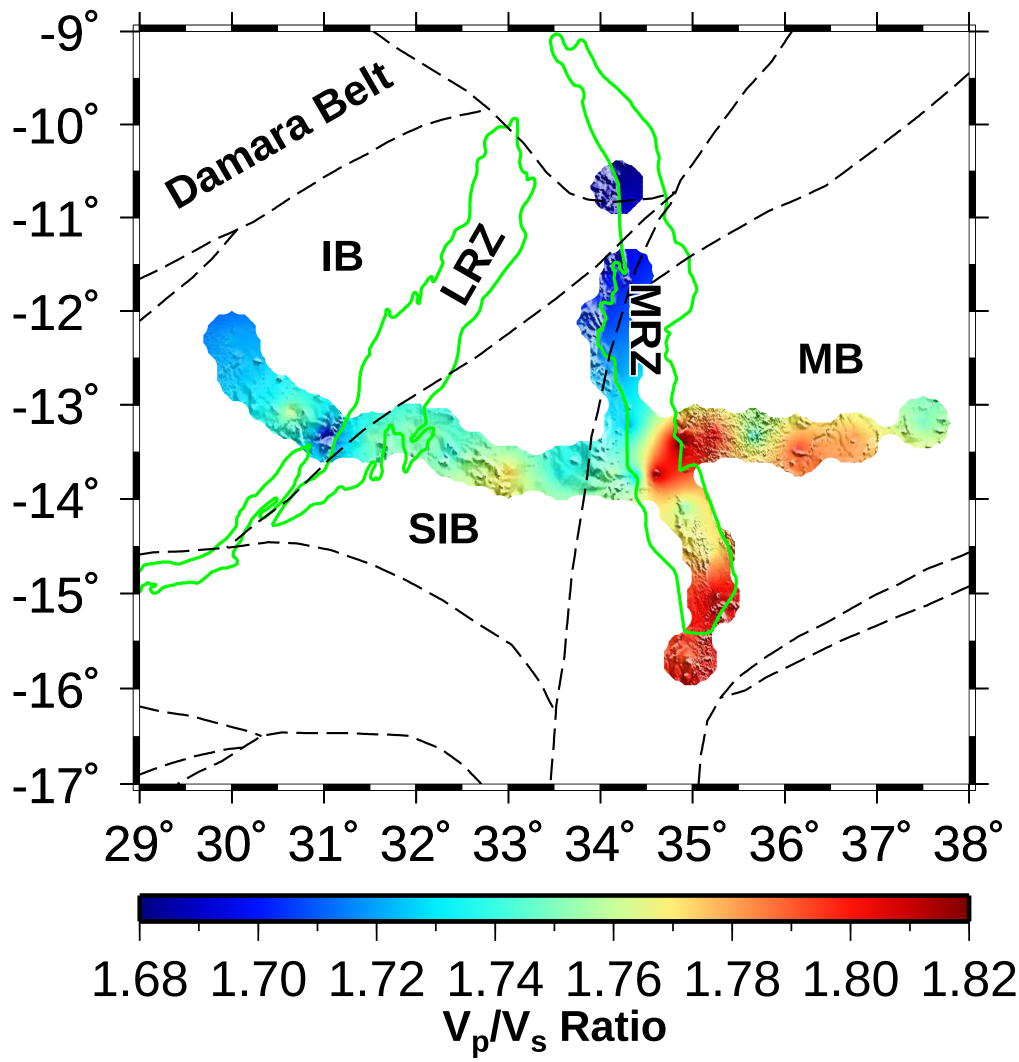

Figure 6. Distribution of resulting V_p/V_s measurements.

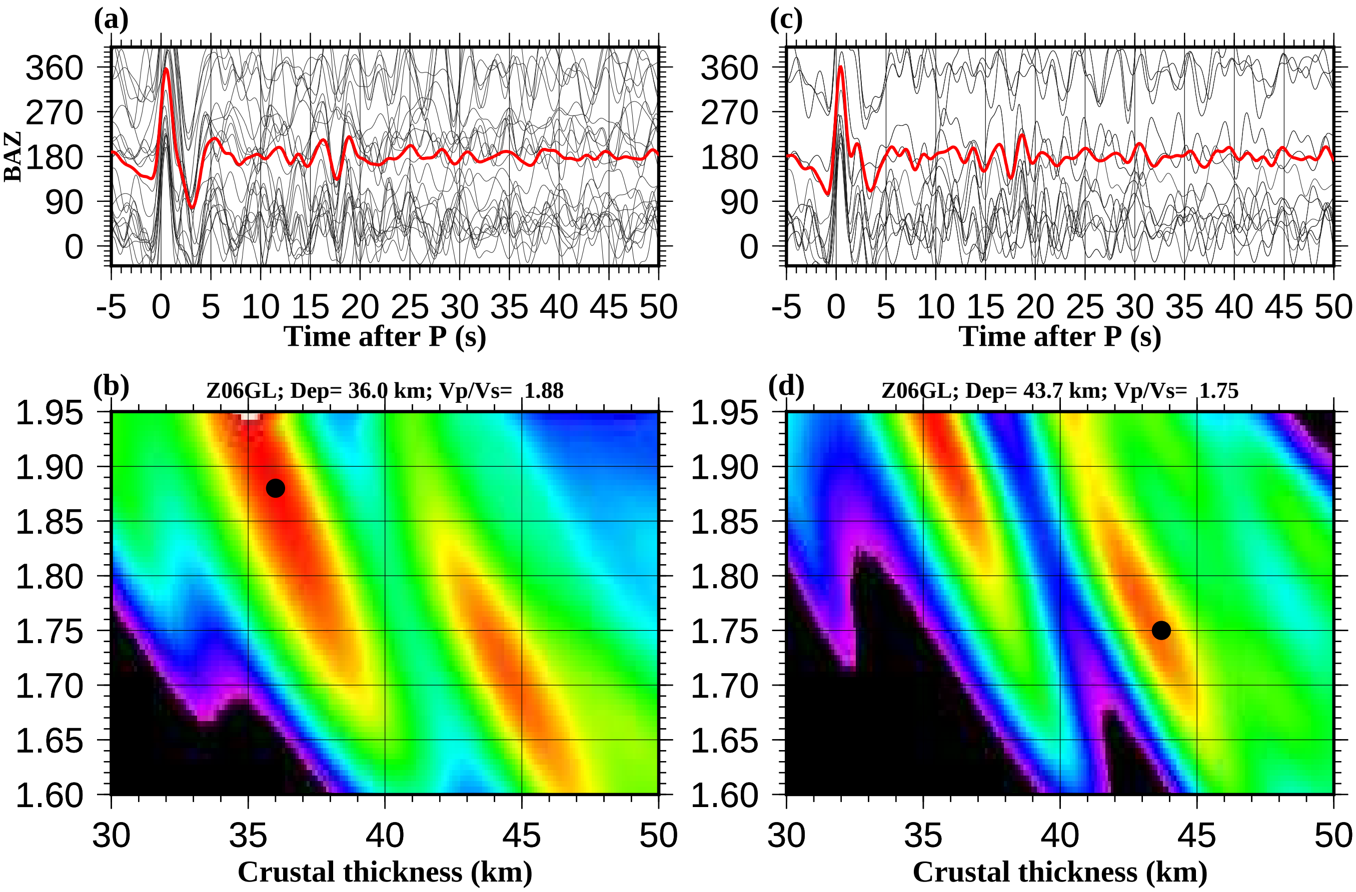

Figure 7. (a) Original RFs from station HENM plotted against back azimuth (BAZ). The red trace is the result of simple time domain summation of the individual RFs and demonstrates the strong decaying periodic arrivals of the reverberations. (b) H-κ stacking using the raw RFs shown in Figure 7a. The dot denotes the maximum stacking amplitude. (c) Same as Figure 7a but for RFs after removing the reverberations using the approach of Yu et al. (2015). (d) H-κ stacking using the filtered RFs shown in Figure 7c.